Supplementary Information

Multimodal human-in-the-loop artificial intelligence with affective feedback for accelerated high-entropy alloy discovery

Jun Jiang[a], Jing Qian[a] , Renchi Xue[b] , Junsong Wang[a], Yanzhi Fu[c], Ziye Xia[a] Fuhan Huo[a], Yiming Zhou[c], Weixin Pan[a], Heng Wang[a], Bin Liu[d], Qihong Fang[a*], Jia Li[a*]

[a] *College of Mechanical and Vehicle Engineering, Hunan University, Changsha, 410082, PR China*

[b] *School of Computer Science and Electric Engineering, Hunan University, Changsha, 410082, PR China*

[c] *School of Artificial Intelligence and Robotics, Hunan University, Changsha, 410082, PR China*

[d] *State Key Laboratory of Powder Metallurgy, Central South University, Changsha, 410083, PR China*

**Corresponding author. E-mail address: fangqh1327@hnu.edu.cn, and lijia123@hnu.edu.cn.*

This file includes:

Supplementary Text 1. Database development for information extraction of HEA

To construct the knowledge base for the information extraction module, We designed a specialized instruction template for the HEA domain to guide the model in identifying and extracting critical information. Each data sample was formatted using few-shot prompts, which enabled the model to learn to extract relevant parameters. For each selected paper, fifteen pieces of information are extracted, which includes bibliographic information (title, abstract, authors, publication year, journal, and DOI) and core data of the article (material, composition, testing condition, phase, research method, content of the study, performance indicators, innovation point, and conclusion). The former serves as a key for article identification, while the latter represents the focus of our analysis. To ensure the high quality of data entries, we implemented a strict multi-step preprocessing workflow: (1) Using DOI as a unique identifier, we identified and merged redundant entries that might appear multiple times in different literature retrieval queries; (2) Entries with missing core data of the article were manually supplemented by domain experts; if the information could not be recovered, "Null" was filled in to ensure entry integrity; (3) All data were organized into key-value pairs and stored in JSON documents to facilitate the training and retrieval of downstream models.

Supplementary Text 2. Extended technical details

2.1 Model training dynamics

The training process was monitored via loss and learning rate curves (Fig. S5). A rapid decrease in loss values within the first 10 epochs indicated efficient initial learning, followed by a gradual stabilization of both training and validation losses. The close alignment between these losses throughout training confirms strong model generalization without overfitting. Optimization employed a cosine annealing scheduler with a warm-up phase. The learning rate increased during an initial ~25-epoch warm-up period to a peak, fostering rapid progress, before decaying via a cosine curve to enable fine-grained convergence. The stable, coordinated evolution of the loss and learning rate curves validates the effectiveness of the training strategy, resulting in a robust and efficient optimization process.

2.2 Detailed SHAP interpretation for Young's modulus prediction

The dominance of VEC is explained by its control over phase selection: VEC < 6.87 favors BCC, VEC > 8 favors FCC, with BCC phases exhibiting higher modulus due to stronger covalent bonding [1]. Element-specific roles: Ti and Zr act as BCC stabilizers. Zr (radius 160 pm) contributes significantly to lattice distortion, indirectly increasing modulus by hindering dislocation motion [2]. Electronegativity difference drives local charge redistribution (e.g., in Al-Ti/Zr pairs), forming strong polar bonds that resist elastic deformation more effectively than geometric distortion alone. The composite feature *Mixing Entropy* × *VEC* highlights synergy: entropy stabilizes the solid solution, while VEC fine-tunes phase selection for optimal stiffness.High-melting-point elements (Mo, W, Nb) enhance bonding via d-orbital participation, directly increasing elastic constants (e.g., shear modulus in BCC phases) [3].

2.3 Detailed SHAP interpretation for yield strength prediction

Niobium is the top contributor due to severe lattice distortion from its large atomic size (radius 1.46 Å) and its tendency to segregate to grain boundaries, pinning dislocations [4]. Atomic radius difference generates substantial lattice distortion energy (~0.75 eV/atom for a 4.6% difference), elevating the Peierls-Nabarro stress (up to 200 MPa) and hindering dislocation motion [5]. The "enthalpy-entropy competition": Negative mixing enthalpy favors stable solid solutions, while mixing entropy promotes single-phase formation; their lower relative importance suggests kinetic effects (short-range order) outweigh pure thermodynamic entropy in strengthening. The Electronegativity difference × Atomic radius difference product captures nano-scale clustering (e.g., Ni-Al pairs), inducing a precipitation-like strengthening effect. A high Young's modulus strengthens the lattice against dislocation nucleation by increasing phonon stiffness. Synergy of specific elements: Zr causes shear modulus fluctuations (±15%) due to its large radius (1.60 Å); Ni reduces stacking fault energy (SFE < 30 mJ/m²) promoting nano-twinning; Cr segregation to grain boundaries inhibits crack propagation.

2.4 Region-wise quantitative interpretation for interaction plots

To avoid overloading the main text, we provide here the detailed region-wise thresholds and representative numeric values used to describe the interaction patterns in Fig. 2g-h. Based on Fig. 2g, the pattern of synergistic regulation of elastic modulus (E) by electronegativity difference (ΔEN) and atomic radius difference (ΔR) is clearly presented: *Low-modulus stability zone (ΔR > 8, ΔEN < 10)*: E stabilizes at 132-135 GPa (e.g., 134.8 GPa at ΔR=9.3), dominated by atomic size mismatch. *Peak-stiffness region (ΔEN=25.8-33.8, ΔR=2.3-3.3)*: Maximum E values (160-164 GPa) occur at ΔEN=29.8/ΔR=3.3 (164.15 GPa), where electronegativity-driven charge redistribution synergizes with controlled lattice distortion. *Gradient transition belt (ΔEN=17.8-21.8)*:

E increases 28% (132→169 GPa) as ΔR decreases from 9.3 to 0.3, demonstrating atomic size matching as the stiffness determinant. Critically, the stiffness enhancement window (ΔEN=25.8-33.8, ΔR=2.3-3.3) exhibits a 10+ GPa modulus gain per 5-unit ΔEN increase, quantifying cooperative bond-strengthening effects.

Fig. 2h reveals the non-monotonic synergistic effect of mixed entropy (ΔS) and valence electron concentration (VEC) on yield strength (YS). *High-strength plateau (VEC < 5)*: YS sustains >1300 MPa (e.g., 1357 MPa at VEC=3.6/ΔS=17), minimally affected by ΔS (7-17 $J \cdot mol^{-1} \cdot K^{-1}$). *Critical collapse zone (VEC=5.8-9.8, ΔS=10-12)*: YS drops 30% to 980-1100 MPa, reaching a minimum (1008 MPa at VEC=7.3/ΔS=10). *Entropy-compensated strengthening (VEC>9.8, ΔS>14)*: YS recovers to 1300-1357 MPa (peak 1357 MPa at VEC=9.5/ΔS=17), confirming entropy-mediated reversal of VEC softening. The inflection point (VEC=7.3) shows each 1 $J \cdot mol^{-1} \cdot K^{-1}$ ΔS increase elevates YS by ≈ 40 MPa (349 MPa gain at ΔS:10→17). This establishes an entropic pinning pathway for high-VEC alloys (>9.5): optimizing strength at ΔS > 14 $J \cdot mol^{-1} \cdot K^{-1}$.

Supplementary Text 3. Human-computer interaction module design

Based on the integrated materials design system, this section focuses on the proposed human-computer interaction (HCI) module, which follows the core logic of dynamic perception-real-time feedback-closed-loop optimization. The module aims to achieve bidirectional collaboration between users and the AI system through multimodal interaction technologies, including voice input, emotion recognition, and visual feedback.

3.1 Key components of the module

*Multimodal Input Interface***.**

Voice Command Parsing: User voice commands (e.g., "prioritize yield strength optimization") are captured in real time via browser-native speech recognition APIs. Semantic parsing is performed by integrating domain knowledge bases (e.g. composition rules of high-entropy alloys) to generate structured query requests.

Emotion State Mapping: User emotion scores (1-5) are quantified in real time through facial expression recognition (face-api model) and acoustic feature analysis (e.g., fundamental frequency, rhythm), which are dynamically injected into the optimization algorithm’s weight parameters.

Intelligent Decision Engine.

Dynamic Weight Adjustment: User emotion scores are converted into objective function weight adjustment factors, driving a novel NSGA-II algorithm to balance performance metrics (YS, E) and user preferences during Pareto front exploration. Real-Time Optimization Trigger: When emotion scores $\leqslant 2$ or voice commands request re-optimization, the system automatically enhances population diversity to avoid local optima. Integrated Extraction-Optimization:

This system seamlessly integrates key information extraction, critical property prediction, and composition system optimization directly from scientific texts. By unifying these three functionalities, the framework significantly broadens its user base, enabling both novices and experts to efficiently obtain tailored assistance for their specific research or application needs.

3.2 Design principles and innovations

Real-Time Assurance.

Computationally intensive tasks (e.g., NSGA-II optimization) are decoupled from interaction tasks using Web Worker multithreading technology, ensuring interface response times <100 ms.

Multimodal Fusion.

A pioneering "emotion-voice-visualization" tri-channel interaction mechanism is proposed, where emotion feedback and voice commands collaboratively regulate optimization directions, significantly improving user satisfaction compared to single-modality systems.

Scalable Architecture.

The modular design enables rapid adaptation to other material systems (e.g., battery electrode materials) by updating feature databases and domain-specific knowledge parsing rules.

3.3 Speech interaction module

Fig. S4(a) shows the Speech interaction module. It employs a real-time stream processing architecture that integrates native browser speech recognition APIs with asynchronous front-end programming models, constructing an end-to-end speech input parsing system. This system comprises three hierarchical layers: speech capture,

recognition-parsing, and error control, achieving comprehensive audio-to-text conversion through multithreading coordination.

During the speech capture phase, the system accesses browser media device layers via the WebKitSpeechRecognition interface, invoking the underlying AudioContext API to acquire microphone audio streams [6]. An event-driven mechanism enables real-time speech signal acquisition, configured with appropriate sampling rates (Hz) and mono-channel audio streams to meet speech recognition engine specifications. Intermediate result feedback is disabled to ensure full-sentence recognition triggered exclusively by endpoint detection, thereby minimizing redundant computational overhead.

Upon audio stream acquisition, the system initializes a speech recognition engine instance using the standard Web Speech API. While the current implementation is optimized for Mandarin Chinese (zh-CN) as a proof of concept, the API inherently supports multiple languages (e.g., English 'en-US'). The recognition language can be easily configured by setting the corresponding language code, ensuring broad international accessibility and adaptability. The system then selects optimal transcription texts. The workflow encompasses acoustic feature extraction, phoneme alignment, and context-aware word graph search based on n-gram language models [7], ultimately generating textual sequences for linguistic-to-text conversion [8].

The error control layer implements dual-level fault tolerance:

(1) Automatic reconnection via exponential backoff strategies handles capture device permission exceptions, network interruptions, and engine internal errors [9].

(2) UI feedback components (ElMessage) deliver real-time error codes and user guidance.By leveraging Web Workers to migrate speech recognition tasks to background threads, the system prevents main-thread blocking-induced interaction latency, ensuring

interface response times remain below 100 ms [10].

3.4 Emotion recognition module

Fig. S4(b) shows the emotion recognition module. It employs the Face-API model, adopting a cascaded multimodal processing architecture [11] that integrates computer vision and deep learning technologies to construct an end-to-end emotion analysis system. This model consists of two hierarchical layers: a facial information perception layer and an emotion pattern matching layer, achieving comprehensive emotion classification through multi-stage feature propagation [12] from face detection to emotion categorization.

During facial information acquisition, the system first captures camera video streams via browser APIs. Utilizing an SSD (Single Shot Multibox Detector) architecture [13] based on the MobileNetV1 feature extraction network, it generates candidate bounding boxes through a sliding window approach and filters regions with confidence scores exceeding predefined thresholds to localize facial areas.

Following facial localization, the model invokes a lightweight dlib-based keypoint detection model [14], which returns coordinates for 68 facial landmarks, including eye contours, eyebrow arches, and mouth boundaries, forming a structural facial mesh. The system applies affine transformation to align faces and normalize pose variations, ensuring standardized inputs for subsequent analysis.

After processing facial data, the system activates a convolutional neural network (CNN)-based emotion classification model [15], which calculates probability distributions across seven emotional states (e.g., happiness, sadness, anger) and selects the highest-probability emotion as the dominant output. This emotional weight is then integrated into downstream decision-making modules to guide adaptive processing.

The emotion recognition module innovatively implements a cascaded "detect-align-classify" pipeline, progressively reducing computational complexity—for instance, performing coarse face detection before fine-grained feature analysis. Technical optimizations include replacing standard convolutions with depthwise separable convolutions, reducing computational costs by approximately 75%, and integrating feature pyramids within the SSD framework to enhance detection accuracy through multi-scale feature map fusion. For emotion classification, a 3-5 layer CNN architecture extracts texture features from critical regions (e.g., eye corners, mouth edges). Additionally, WebGL backend utilization enables GPU-accelerated parallel computing to optimize inference speeds.

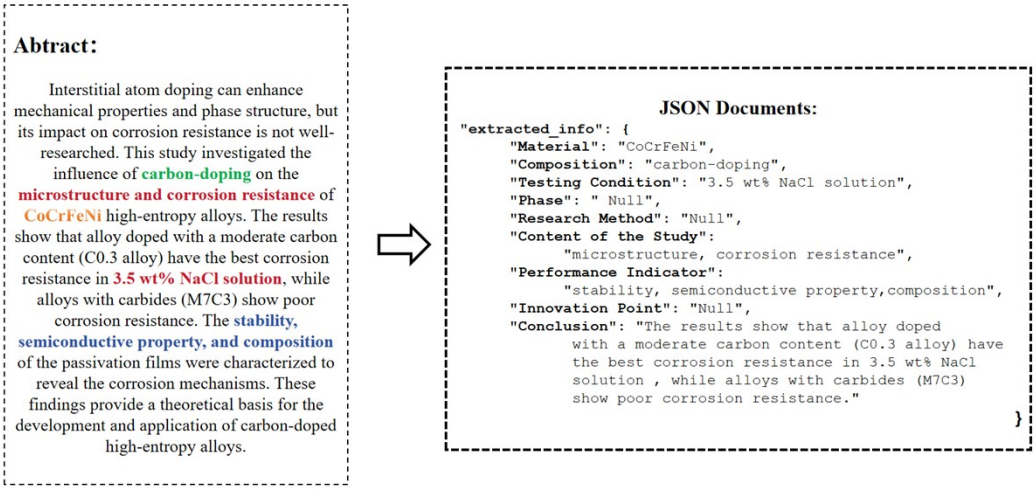

Figure S1. Workflow of information extraction for HEA literature database construction.

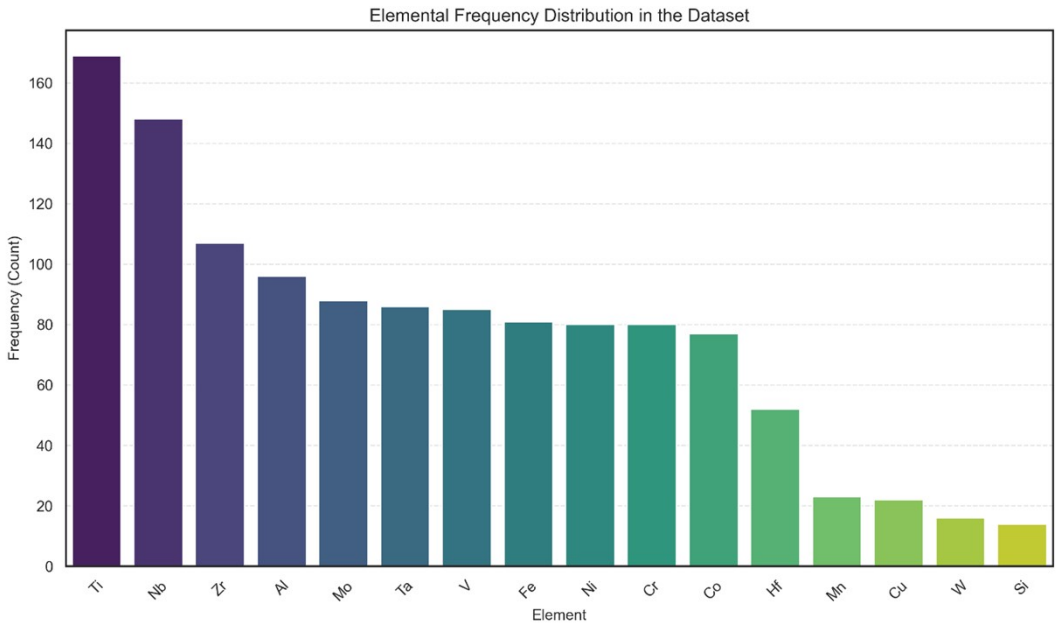

Figure S2. Frequency distribution of constituent elements in the dataset. The histogram illustrates the occurrence count of primary elements (including Ti, Nb, Zr, Al, Mo, Ta, V, Fe, Ni, Cr, Co, etc.), demonstrating that the dataset provides a representative coverage of the compositional space for transition metal high-entropy alloys despite its focused size.

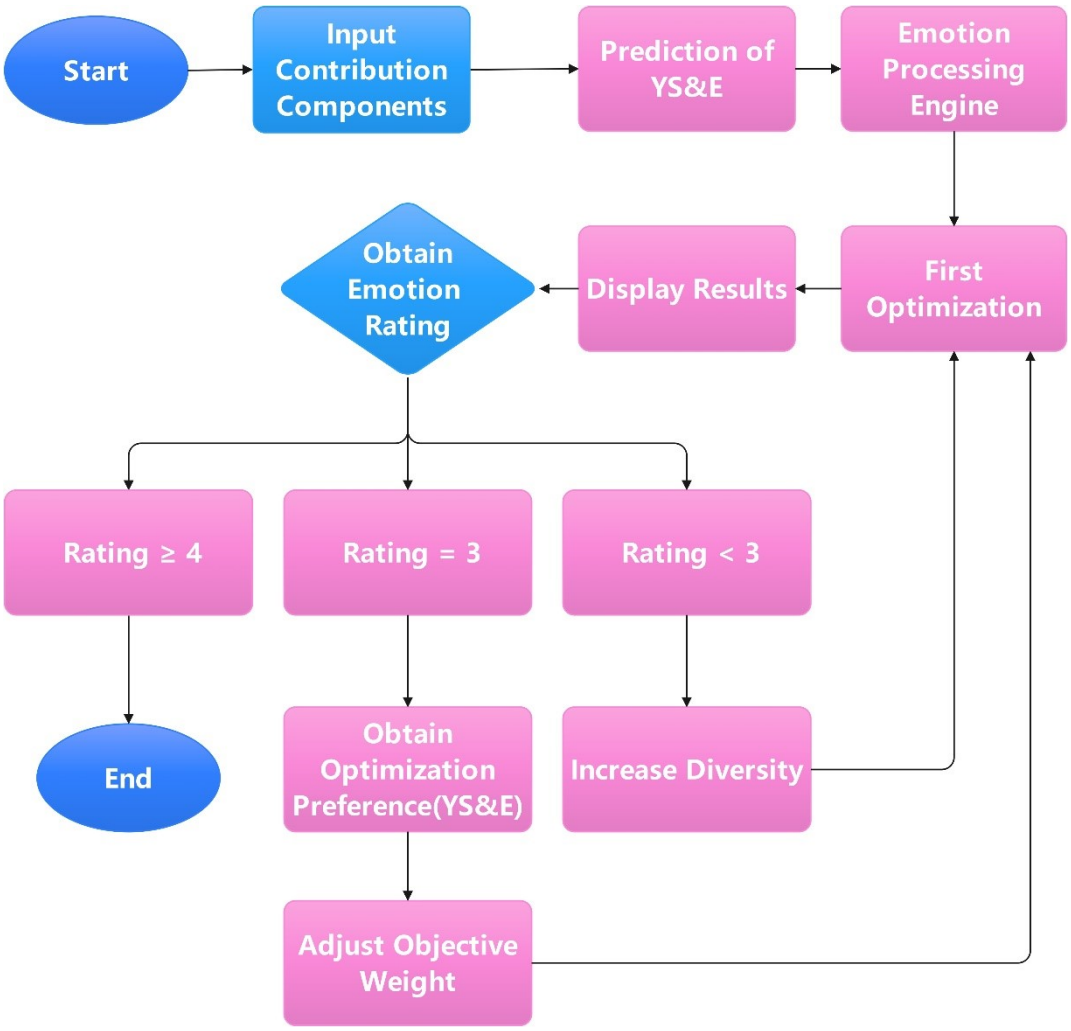

Figure S3. The flowchart of the algorithm of component optimization.

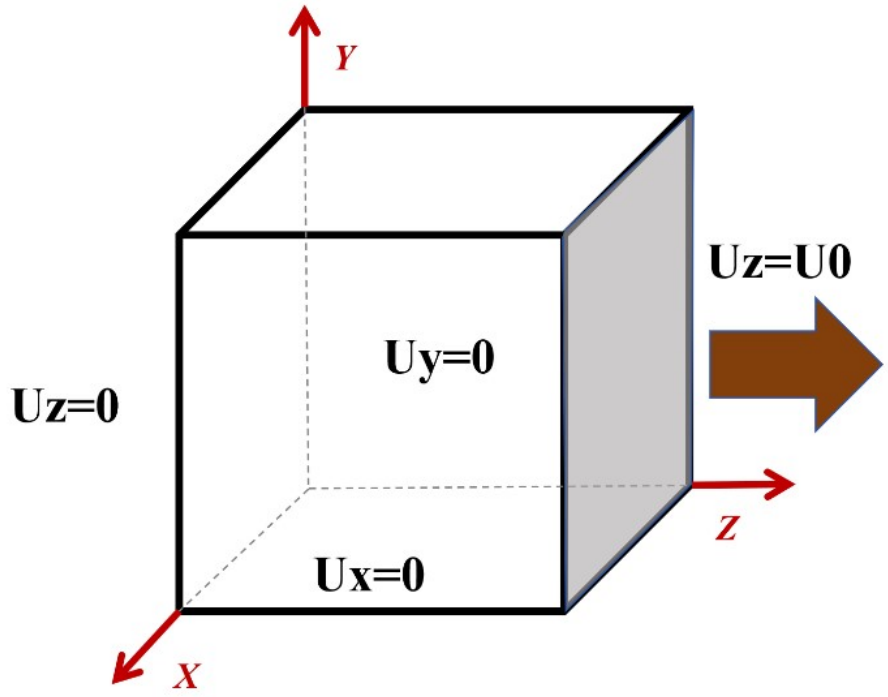

Figure S4. Schematic diagram of boundary condition.

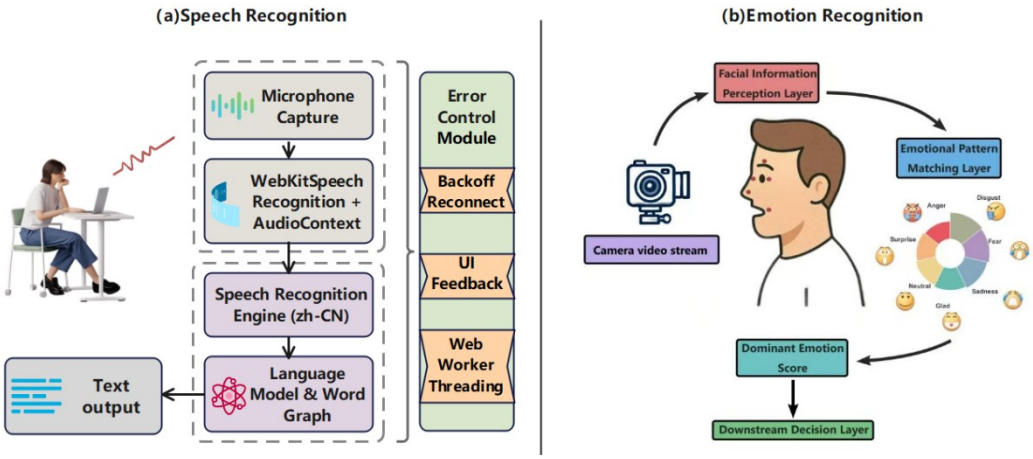

Figure S5. Schematic diagram of the principle of speech recognition and emotion recognition module**.** **a.** Speech Recognition: Microphone captures sound waves which will be recognized and be processed by speech recognization engine, then model generate text output. **b.** Emotion Recognition: Facial data from video is analyzed in perception and matching layers to identify emotional patterns. The dominant emotion score guides downstream decisions.

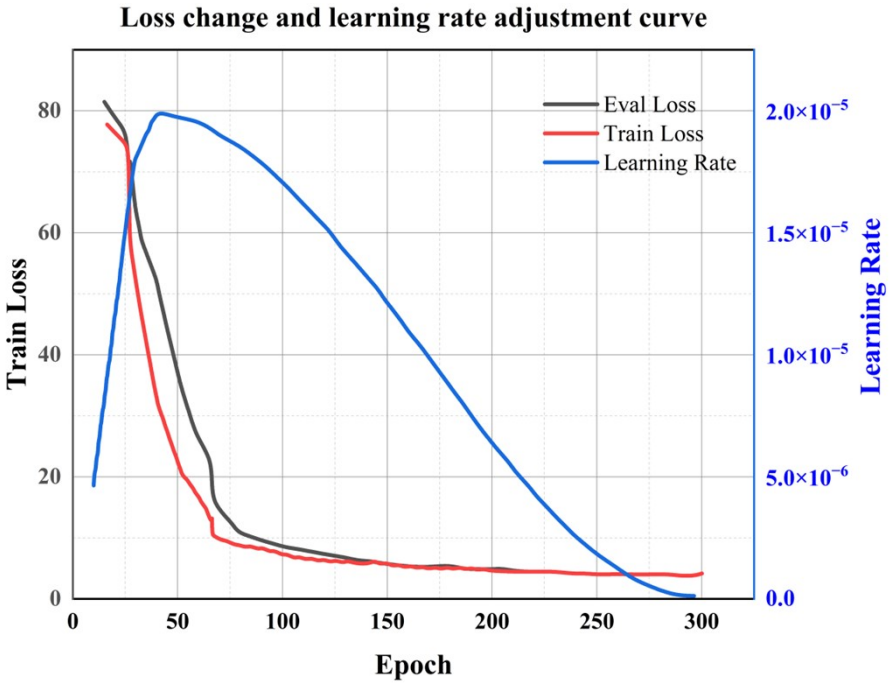

Figure S6. Loss change and learning rate adjustment curve.

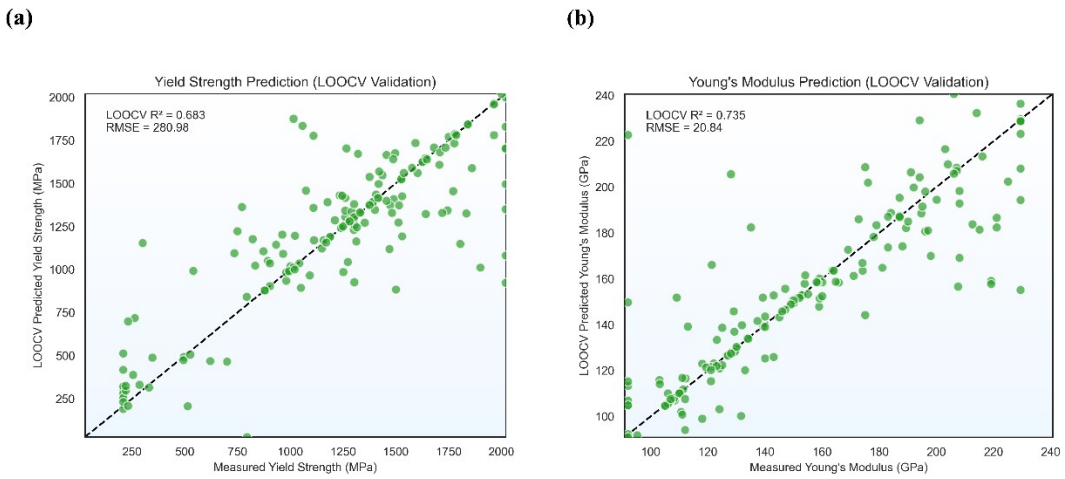

Figure S7. Leave-One-Out Cross-Validation (LOOCV) assessment of model robustness. Parity plots comparing the experimentally measured values against the LOOCV predicted values for (a) Yield Strength (R2=0.683, RMSE=280.98 MPa) and (b) Young's Modulus (R2=0.735, RMSE=20.84 GPa).

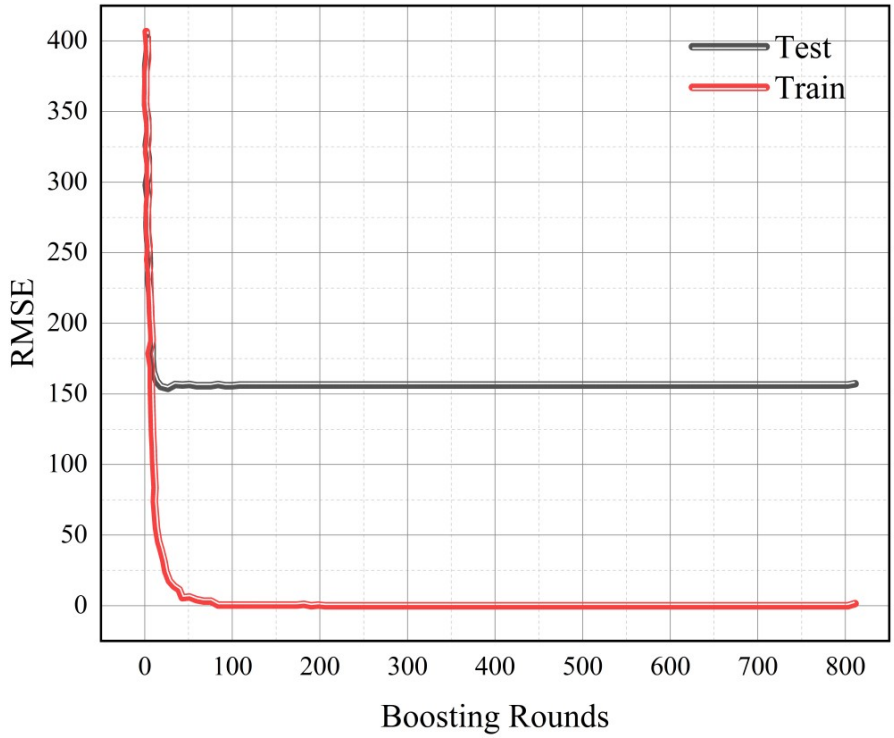

Figure S8. RMSE of the YS model regarding changes in boosting rounds.

RMSE decreases rapidly in the first 100 generations and then stabilizes. There is a reasonable difference between the training set and the test set, with the training set having a significantly higher accuracy than the test set.

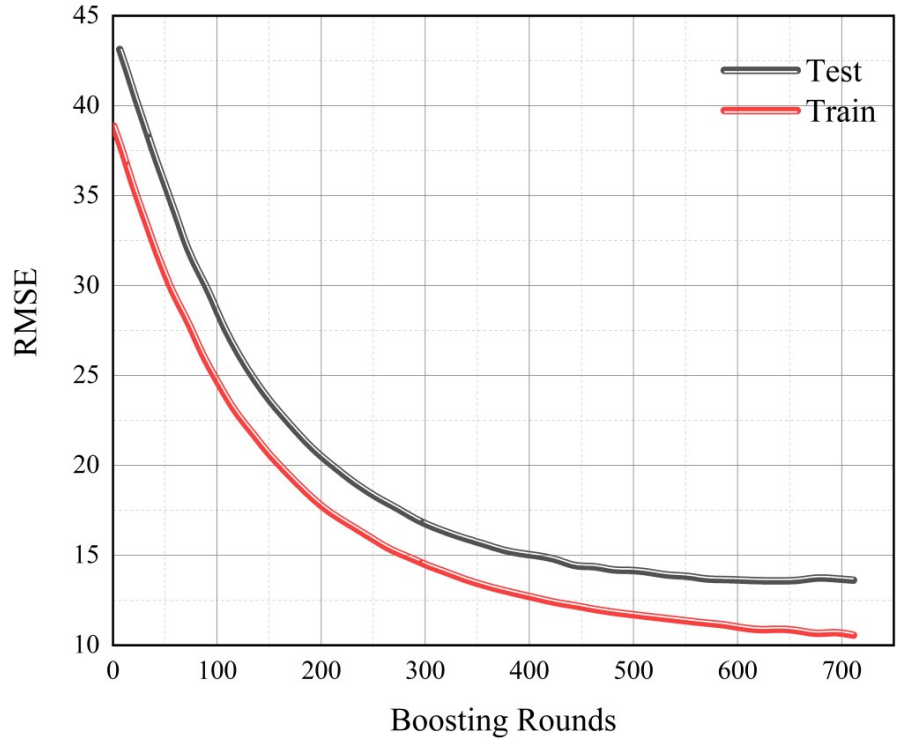

Figure S9. RMSE of the E model regarding changes in boosting rounds.

RMSE decreases rapidly in the first 400 generations and then stabilizes. There is a reasonable difference between the training set and the test set. In the E model, the accuracy of the training set is slightly higher than that of the test set, demonstrating that the model has high accuracy.

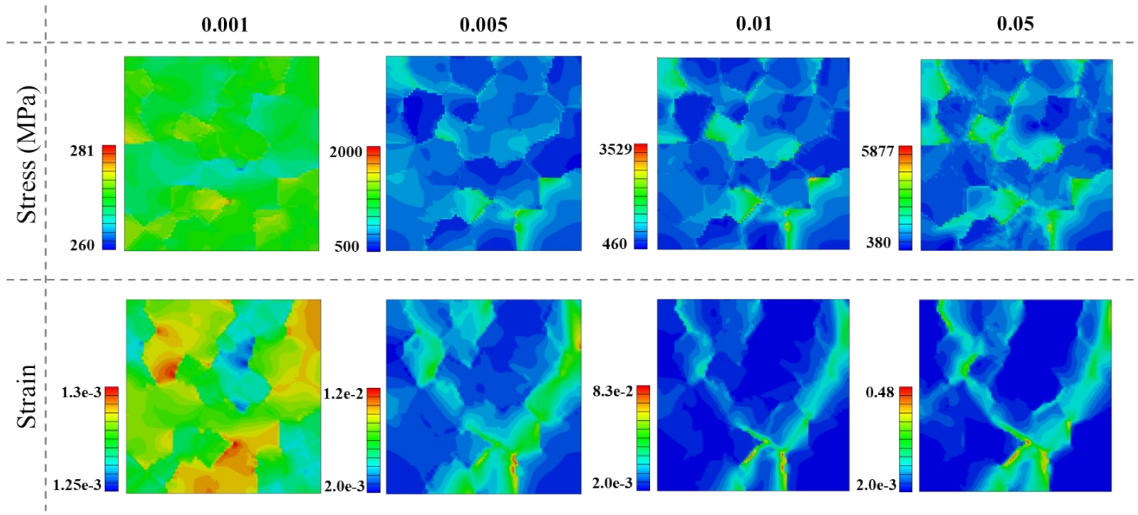

Figure S10. Strain distribution of the $AlCoCrFeNi_{2.1}$ HEA at the strain of 0.1 % (elastic stage), 0.5 % (yielding stage), 1 % and 5 % (plastic stage).

Table S1. Some of the data used for performance prediction [16-28].

HEA Composition	Mixing Entropy	Mixing Enthalpy	Young's modulus
$Al_{0.2}CoCrFeNi$	12.56	-6.21	216
$Al_{0.45}CoCrFeNi$	13.08	-8.66	208
$Al_{0.7}CoCrFeNi$	13.30	-10.57	200
AlCoCrFeNi	13.38	-12.32	387
AlHfNbTaTiZr	14.89	-15.77	103
$AlMo_{0.5}NbTa_{0.5}TiZr$	14.53	-18.28	122
$AlMo_{0.5}NbTa0.5TiZr_{0.5}$	14.42	-17.58	133
AlMoNbTiV	13.38	-12.8	149.6
AlMoTaTiV	13.38	-12.96	165.8
$AlNb_{1.5}Ta_{0.5}Ti_{1.5}Zr_{0.5}$	12.51	-16.2	105.7
$AlNbTa_{0.5}TiZr_{0.5}$	12.96	-19.68	124
AlNbTaTiV	13.38	-13.44	121
AlNbTiV	11.52	-16.25	104.8
CoCrFeNi	11.52	-3.75	225
CoCrFeNiTi	13.38	-16.32	135
AlCoCrFeNi	13.38	-12.32	194
$AlCoCrFeNiSi_{0.2}$	14.22	-16.39	188
$AlCoCrFeNiSi_{0.4}$	13.01	-18.14	183
$AlCoCrFeNiSi_{0.6}$	14.77	-22.75	178

Table S2. The parameters of CPFE model.

Symbol	Parameter	Value	
		FCC	BCC
Burgers vector (Å)	b	2.52 [29]	2.50 [29]
initial dislocation density (m^{-2})	ρ_0	1.20×10^{13} [30]	1.40×10^{14} [31]
Initial hardening parameter (MPa)	h_0	345.0	705.0
Saturated slip resistance (MPa)	S_s	1450.0	2950.0
Reference shearing rate (s^{-1})	$\dot{\gamma}_0$	10^{-3} [32]	
Strain rate sensitivity exponent	n	0.04	
Latent-hardening parameter	q	1.4 [33]	
CRSS (MPa)	τ_{sr}	255.0	793.0
Sensitivity of hardening moduli	r	2.25	2.0
Elastic constants (GPa) [34]	C_{11}	289.0	291.7
	C_{12}	124.0	125.0
	C_{44}	82.7	83.4

Table S3. The representative hyperparameters used to train the XGBoost model.

Hyperparameter	Optimization Range / Value
learning_rate	1×10^{-4} ~0.3(log-uniform)
max_depth	8 ~15
n_estimators	500 ~2000
subsample	0.6 ~1.0
colsample_bytree	0.4 ~1.0
gamma	0 ~2

Table S4. The hyperparameters for classical NSGA-II algorithm.

Hyperparameter	Value
pop_size	100
crossover_prob (SBX)	0.9
crossover_eta (SBX)	15
mutation_eta (PM)	20
termination	200

Supplementary Data 1

The complete dataset used for the training and testing of the information extraction model for HEAs. This file comprises data extracted from 250 papers, including alloy compositions (Al, Co, Cr, Fe, Ni, etc.), processing conditions, and mechanical properties (yield strength and Young's modulus). The data is provided in Microsoft Excel (.xlsx) format.

References

[1] Guo, S. Phase selection rules for cast high entropy alloys: An overview. *Mater. Sci. Technol.* 31, 1223–1230 (2015).

[2] Huang, W. et al. Microstructures and mechanical properties of TiZrHfNbTaWx refractory high entropy alloys. *J. Alloys Compd.* 914, 165187 (2022).

[3] Li, X. Phase stability and micromechanical properties of TiZrHf-based refractory high-entropy alloys: A first-principles study. *Phys. Rev. Mater.* 7, 113604 (2023).

[4] He, F. et al. Designing eutectic high entropy alloys of CoCrFeNiNbx. *J. Alloys Compd.* 656, 284–289 (2016).

[5] Lee, C. et al. Lattice distortion in a strong and ductile refractory high-entropy alloy. *Acta Mater.* 160, 158–172 (2018).

[6] Ding, Y. G., Liu, J. & Liu, R. S. Real-time speech recognition algorithm on embedded systems. *J. Signal Process.* 3, 3–5 (2005).

[7] Ma, P., Petridis, S. & Pantic, M. End-to-end audio-visual speech recognition with conformers. *Proc. IEEE Int. Conf. Acoust. Speech Signal Process. (ICASSP)*, 7613–7617 (2021).

[8] Xu, H. K., Lu, J. K., Zhang, Z. F., Zhou, J. J., Hu, W. Y., Jiang, T. T., Guo, W. T. & Li, Z. Y. Chinese speech recognition combining Conformer and N-gram. *Comput. Sci. Appl.* 8, 1–6 (2022).

[9] Clark, H., Jeong, N. S. & Jeong, S. Concurrent gain and bandwidth improvement of a patch antenna with a hybrid particle swarm optimization algorithm. *Proc. IEEE Int. Symp. Antennas Propag.*, 5–11 (2023).

[10] Jouni, M., Picone, D. & Dalla Mura, M. Model-based spectral reconstruction of interferometric acquisitions. *Proc. IEEE Int. Conf. Acoust. Speech Signal Process.*

(ICASSP), 1–5 (2023).

[11] Zhao, S., Jia, G. & Yang, J. Emotion recognition from multiple modalities: fundamentals and methodologies. *IEEE Signal Process. Mag.* 38, 59–73 (2021).

[12] Dai, W., Cahyawijaya, S. & Liu, Z. Multimodal end-to-end sparse model for emotion recognition. *arXiv preprint* arXiv:2103.09666 (2021).

[13] Howard, A. G., Zhu, M. & Chen, B. MobileNets: efficient convolutional neural networks for mobile vision applications. *arXiv preprint* arXiv:1704.04861 (2017).

[14] Li, J., Li, X. & Wei, Y. Multi-level feature aggregation-based joint keypoint detection and description. *Comput. Mater. Continua* 73, 2529–2540 (2022).

[15] Huang, Z., Ma, Y. & Wang, R. A model for EEG-based emotion recognition: CNN-Bi-LSTM with attention mechanism. *Electronics* 12, 3188 (2023).

[16] Li, C., Zhang, Y. & Zhou, F. Effect of aluminum contents on microstructure and properties of $Al_xCoCrFeNi$ alloys. *J. Alloys Compd.* 504, S515–S518 (2010).

[17] Juan, C. H. E., Zhang, Z. Z. & Zhang, L. J. Influence of Al, Cu and Mn additions on diffusion behaviors in CoCrFeNi high-entropy alloys. *Trans. Nonferrous Met. Soc. China* 35, 184–193 (2025).

[18] Lin, C. M., Wang, H. & Chang, C. Effect of Al addition on mechanical properties and microstructure of refractory $Al_xHfNbTaTiZr$ alloys. *J. Alloys Compd.* 624, 100–107 (2015).

[19] Senkov, O. N., Senkova, S. V. & Miracle, D. B. Compositional variation effects on the microstructure and properties of a refractory high-entropy superalloy $AlMo_{0.5}NbTa_{0.5}TiZr$. *Mater. Des.* 139, 498–511 (2018).

[20] Ge, H. & Tian, F. A review of ab initio calculation on lattice distortion in high-entropy alloys. *JOM* 71, 4225–4237 (2019).

[21] Zhu, J. M., Wang, Q. & Li, X. Synthesis and properties of multiprincipal component AlCoCrFeNiSi$_x$ alloys. *Mater. Sci. Eng. A* 527, 7210–7214 (2010).

[22] Munitz, A., Salhov, S. & Hayun, S. Heat treatment impacts the microstructure and mechanical properties of AlCoCrFeNi high entropy alloy. *J. Alloys Compd.* 683, 221–230 (2016).

[23] Fujieda, T., Yamaguchi, T. & Kurosu, S. Mechanical and corrosion properties of CoCrFeNiTi-based high-entropy alloy additive manufactured using selective laser melting. *Addit. Manuf.* 25, 412–420 (2019).

[24] Liu, W. H., Yang, T. & Liu, C. T. Precipitation hardening in CoCrFeNi-based high entropy alloys. *Mater. Chem. Phys.* 210, 2–11 (2018).

[25] Salishchev, G. A., Tikhonovsky, M. A. & Shaysultanov, D. G. Effect of Mn and V on structure and mechanical properties of high-entropy alloys based on CoCrFeNi system. *J. Alloys Compd.* 591, 11–21 (2014).

[26] Stepanov, N. D., Shaysultanov, D. G. & Tikhonovsky, M. A. Structure and mechanical properties of a light-weight AlNbTiV high entropy alloy. *Mater. Lett.* 142, 153–155 (2015).

[27] Guo, W., Liu, L. & Zhang, Y. Microstructures and mechanical properties of ductile NbTaTiV refractory high entropy alloy prepared by powder metallurgy. *J. Alloys Compd.* 776, 428–436 (2019).

[28] Senkov, O. N., Miracle, D. B. & Yang, X. Development and exploration of refractory high entropy alloys — a review. *J. Mater. Res.* 33, 3092–3128 (2018).

[29] Kireeva, I. V., Chumlyakov, Y. I., Pobedennaya, Z. V. & Vyrodova, A. V. Effect of γ′-phase particles on the orientation and temperature dependence of the mechanical behaviour of Al0.3CoCrFeNi high-entropy alloy single crystals. *Mater. Sci. Eng., A* 772,

138772 (2020).

[30] Wang, X., Zhang, Z., Wang, Z. & Ren, X. Excellent tensile property and its mechanism in Al0.3CoCrFeNi high-entropy alloy via thermo-mechanical treatment. *J. Alloys Compd.* 897, 163218 (2022).

[31] Giwa, A. M., Aitken, Z. H., Liaw, P. K., Zhang, Y. W. & Greer, J. R. Effect of temperature on small-scale deformation of individual face-centered-cubic and body-centered-cubic phases of an Al0.7CoCrFeNi high-entropy alloy. *Mater. Des.* 191, 108611 (2020).

[32] Xiong, T., Zheng, S., Pang, J. & Ma, X. High-strength and high-ductility AlCoCrFeNi2.1 eutectic high-entropy alloy achieved via precipitation strengthening in a heterogeneous structure. *Scr. Mater.* 186, 336–340 (2020).

[33] Fang, Q., Lu, W., Chen, Y., Feng, H., Liaw, P. K. & Li, J. Hierarchical multiscale crystal plasticity framework for plasticity and strain hardening of multi-principal element alloys. *J. Mech. Phys. Solids* 169, 105067 (2022).

[34] Zhai, H., Yao, B., Zhang, W., Lin, H., Ma, X., Li, Y. & Wang, S. On the plastic deformation mechanism of Al0.6CoCrFeNi high entropy alloy: In-situ EBSD study and crystal plasticity modeling. *Mater. Sci. Eng. A* 915, 147108 (2024).